RESEARCH



Comparative evaluation of data-based estimators for wave-induced force in wave energy converters

Marcos D. Saavedra¹ · Nicolás Faedo² · Fernando A. Inthamoussou¹ · Facundo D. Mosquera¹ · Fabricio Garelli¹

Received: 20 May 2025 / Accepted: 12 August 2025 © The Author(s) 2025

Abstract

Wave energy conversion technology emerges as a promising approach to renewable energy generation, offering a consistent and predictable power source that complements intermittent renewable energy sources such as solar and wind power. Achieving optimal ocean wave energy absorption requires precise knowledge of the so-called wave excitation force, which is typically estimated through model-based techniques reliant on accurate system descriptions. However, uncertainties inherent to hydrodynamic modelling often limit the reliability of these approaches. To address this challenge, this paper presents a comprehensive evaluation of model-free data-based estimators, for wave excitation torque estimation in Wavestar like wave energy converters (WECs). The study examines various neural network architectures, including static models (feedforward networks) and those incorporating temporal dynamics (recurrent neural networks and long short-term memory networks). The analysis examines the impact of utilising multiple input combinations, ranging from motion variables to configurations enhanced with surrounding wave height measurements from the device's vicinity. Input selection is guided by correlation analysis and spectral coherence evaluation to ensure physical relevance and practical feasibility. Estimators are trained and tested using experimental data obtained from a comprehensive wave tank campaign emulating diverse sea state conditions. The results demonstrate that architectures incorporating temporal considerations achieve superior performance, particularly under wide-banded sea states. A comparative analysis with a model-based estimator, implemented via a Kalman–Bucy Filter with a harmonic oscillator expansion, highlights the advantages of neural networks, especially under challenging conditions where model-based approaches face significant limitations. These findings underscore the capability of data-based strategies to reduce dependence on potentially complex and uncertain analytical models, offering a promising alternative for improving WEC control systems.

Keywords Wave energy converters · Wave excitation force · Data-based estimation · Artificial neural networks

 ⊠ Nicolás Faedo nicolas.faedo@polito.it

> Marcos D. Saavedra saavedramarcosdavid@ing.unlp.edu.ar

Fernando A. Inthamoussou intha@ing.unlp.edu.ar

Facundo D. Mosquera facundo.mosquera@ing.unlp.edu.ar

Fabricio Garelli fabricio@ing.unlp.edu.ar

Published online: 01 September 2025

Instituto de Investigaciones en Electrónica, Control y Procesamiento de Señales - LEICI (UNLP-CONICET), Facultad de Ingeniería, Universidad Nacional de La Plata, La Plata, 1900 Buenos Aires, Argentina

1 Introduction

Achieving carbon neutrality by 2050 stands as a critical and ambitious objective established in recent decades (International Energy Agency 2021), further underscored by the growing emphasis on global energy security in the face of evolving geopolitical landscapes (Wang et al. 2024). Attaining this goal necessitates a substantial increase in the integration of variable renewable energy sources, effectively dominating the energy generation portfolio. Within this context, *ocean wave energy* emerges as a promising renewable source, offering a consistent and predictable baseload supply that complements intermittent resources. Unlike other

Department of Mechanical and Aerospace Engineering (DIMEAS), Politecnico di Torino, Turin, 10129 Turin, Italy



renewable sources, wave energy exhibits no day-night variability, demonstrates seasonal complementarity with solar energy, and often remains statistically uncorrelated with wind resources (Gunn and Stock-Williams 2012). However, the economic viability of wave energy remains hindered due to the currently high Levelised Cost of Energy (LCoE) metrics (Castro-Santos et al. 2015). Over the past decade, advancements in control system technology have been identified as essential in achieving commercial feasibility of wave energy converters (WEC) (Ringwood et al. 2023b). Control engineering plays a decisive role in optimising WEC performance across diverse conversion mechanisms, enabling enhanced energy capture and operational bandwidth without significant capital expenditure. While control methodologies have matured significantly (Scruggs 2024; Ringwood et al. 2023b), optimal energy extraction fundamentally relies on accurately estimating the wave excitation force acting on the device's submerged surface (see, e.g. Faedo et al. 2022). This force constitutes the primary energy source and is integral to both performance optimization and technological constraint satisfaction (Ringwood et al. 2023b). Despite its importance, estimation of this force can be significantly challenging, with prevailing techniques predominantly rooted in model-based formulations (Peña-Sanchez et al. 2019).

The majority of traditional estimation strategies require a model of the WEC, along with an approximate representation of the process to be estimated, typically formulated in implicit terms, consistent with the internal model principle (Francis and Wonham 1976). Examples include harmonic (Hillis et al. 2020; Papini et al. 2024) and random-walk (Nguyen and Tona 2017) formulations, where the dynamical model of the device is extended to incorporate the external variable as part of its internal state representations. While widely adopted in practice, this approach often needs high gains to ensure adequate bandwidth and requires substantial in-situ tuning (García-Violini et al. 2024). Alternatively, a second category of techniques, rooted in disturbance-observer-based control (Chen et al. 2015), avoids the need for an internal model of wave excitation by leveraging the duality between controllers and observers. Essentially, a 'controller' is designed to track the real-time behaviour of the device, thereby estimating the corresponding input force (see, for instance Faedo et al. 2021; Mosquera et al. 2024; Fornaro et al. 2024). This method effectively computes an approximate inverse of the available dynamical model; consequently, any modelling inaccuracies, which are ubiquitous in hydrodynamic modelling (see, for example, Celesti et al. 2025), directly impact the quality of the input estimation. To address the limitations of model-based approaches for reconstructing the excitation force in WECs, machine learning (ML) techniques have been explored as an alternative.

This paper presents a comprehensive evaluation of modelfree data-based estimators for the wave excitation force,

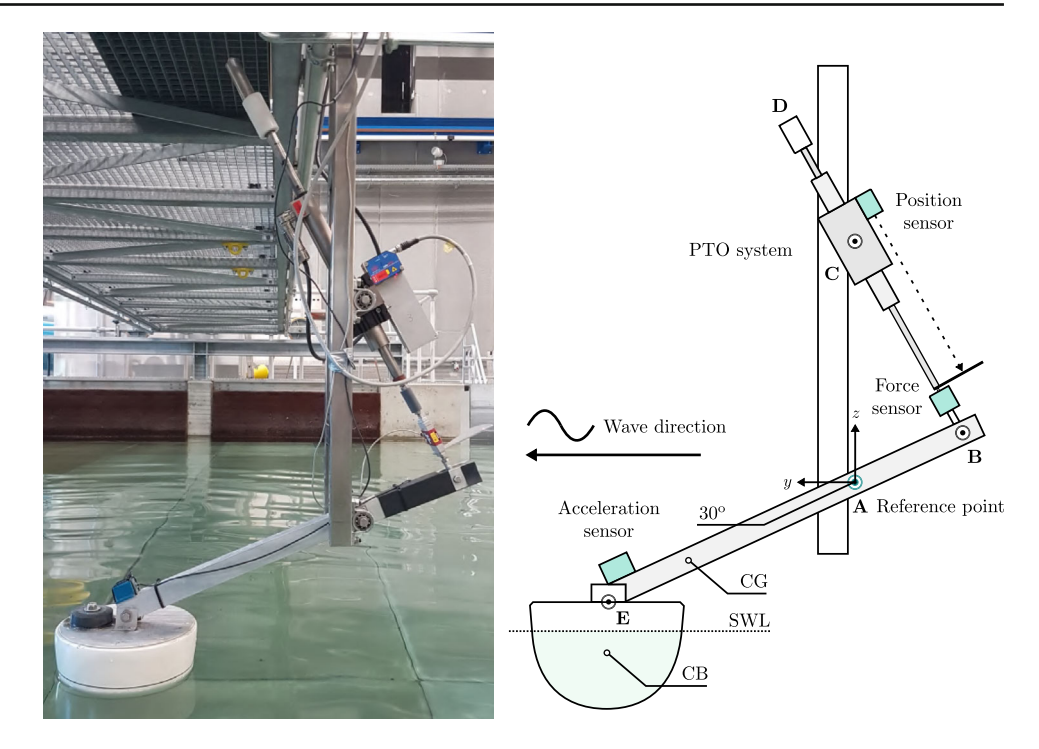
which are based on artificial neural network (NN) and trained using experimental data from a 1:20 prototype Wavestar device (Faedo et al. 2023a). While most ML-based methods to date have been applied for prediction purposes (Masoumi et al. 2024; Zhang et al. 2024a, b; Mahmoodi et al. 2022), to the best of the authors' knowledge, only the work by Bonfanti et al. (2020b, a) has employed ML specifically for the direct estimation of the excitation force. Unlike these studies. which typically focus on individual NN architectures or rely on limited input feature sets, the present work systematically investigates a range of NN architecture types, including static configurations, recurrent structures, and those incorporating temporal considerations. These estimators are organised into distinct groups according to their input configurations, which include WEC motion-related variables and strategically selected surrounding wave height measurements from the vicinity of the device, in order to analyse the impact of incorporating auxiliary variables and the influence of choosing relevant inputs. Feature selection process is guided by correlation analysis and signal availability criteria to ensure practical relevance. Additionally, a spectral coherence analysis is leveraged to identify frequency-dependent relationships between inputs and the target variable, ensuring the inclusion of physically meaningful features while considering practical sensor availability constraints. This structured evaluation provides critical insights into the trade-offs between model complexity, input informativeness, and estimation accuracy in real-world wave energy applications. Furthermore, the proposed data-based methodologies are compared against an estimator based on Kalman-Bucy filter (KBF) with a harmonic oscillator (HO) expansion. This specific linear¹ observer is considered as a benchmark case for comparison, since it constitutes the standard approach adopted within the literature of model-based wave excitation estimation with the scope of control applications Peña-Sanchez et al. (2019); Bonfanti et al. (2020b); Ringwood et al. (2023a). Note that within the same KBF framework, different internal models for the description of the wave excitation process can be considered, by replacing the harmonic implicit form by e.g. a random walk representation.

Unlike the previous study, experimental validation of all estimators is performed through diverse sea states derived from the testing campaign reported in Faedo et al. (2023a). The results are systematically analysed to assess robustness under varying spectral conditions, highlighting the effectiveness of the proposed approach in handling complex maritime environments.



¹ Nonlinear model-based observers have also been considered for the application (see, for instance, Fusco and Ringwood (2012)), yet these come with specific drawbacks regarding the convergence of estimates and the computational effort required to provide wave excitation force values in real-time (see Peña-Sanchez et al. (2019)).

Fig. 1 1:20 scale prototype for the Wavestar converter



The remainder of this work is organised as follows. Section 2 describes the experimental setup for data acquisition, including the definition of the operating conditions and main variables exploited in training and validation. Section 3 details the data-based techniques proposed for wave excitation estimation, while Sect. 4 provides a comprehensive assessment of the performance achieved by each strategy. Subsequently, Sect. 5 offers an in-depth analysis of the results. Finally, Sect. 6 encompasses the main conclusions and future directions arising from this research.

2 Experimental setup for data acquisition

This section provides a brief overview of the experimental configuration and WEC prototype utilised to generate the dataset employed in this work for training and validating the proposed estimation methods. In particular, the experimental setup is designed for the WEC array campaign presented in Faedo et al. (2023a), with the corresponding data accessible in an open-source format in Faedo et al. (2023b).

2.1 Prototype and basin

The chosen baseline WEC system is a 1:20 scale model of the Wavestar (Hansen and Kramer 2011). A single unit of this prototype, illustrated in Fig. 1, primarily consists of a floater that is mechanically connected via a hinge to a fixed reference point above the water surface (see point **A** in the prototype image). The floater's arm maintains an inclina-

tion of approximately 30° with respect to the still water level (SWL) in its equilibrium position. Note that this device operates in a single degree of freedom (DoF), i.e. pitch motion about the reference point $\bf A$.

The device is equipped with a direct-drive linear motor positioned at the upper structural joint of the device (see Fig. 1), which is used within Faedo et al. (2023a) as a power take-off (PTO) unit. Although the PTO system inherently provides translational displacement as an output, an additional measurement is available (for redundancy) using a laser position sensor. The total force along the PTO axis is recorded through a dedicated load cell. To complement these measurements, a dual-axis accelerometer is mounted on top of the floater. This sensor, in conjunction with translational motion data, facilitates the derivation of rotational motion parameters (i.e. angular displacement and velocity) about the fixed reference point A. Data acquisition is performed at a sampling frequency of 200 [Hz] for all recorded variables.

The experimental campaign has been conducted at the Ocean and Coastal Engineering Laboratory at Aalborg University, Denmark. The wave tank facility, illustrated schematically in Fig. 2, consists of a 19.3 m \times 14.6 m \times 1.5 m basin, with an active test region measuring 13 m \times 8 m. The tank features a state-of-the-art, long-stroke, segmented wavemaker system comprising 30 independently controlled paddles with active absorption, enabling precise replication of various sea state conditions. The water depth is set to 0.9 m, and the wavemaker is configured to generate long-crested



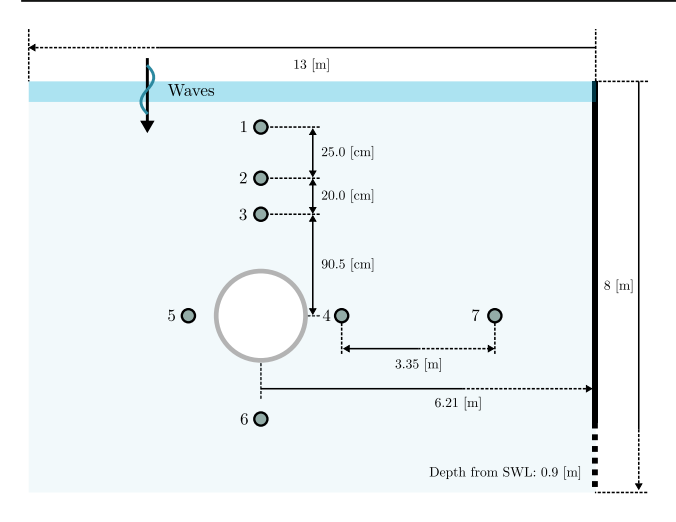


Fig. 2 Schematic representation of the testing setup and basin. Wave probes are illustrated using small grey dots

waves propagating along the x-axis, with a direction of 0° relative to the y-axis, as indicated in Fig. 2.

Free-surface elevation measurements are obtained using resistive-type wave probes (WPs), with seven probes strategically distributed within the wave tank. The subset of WPs {1, 2, 3} is arranged in a column-like configuration along the device's centreline, with varying spacings to facilitate the detection of radiated waves reflected from the tank walls. Additionally, WPs 4 and 5 are positioned along the device's centreline to directly capture the radiated waves generated by the motion of the WEC. WP 6 is located downstream, behind the device relative to the wave propagation direction, while WP 7 serves as a reference probe, placed outside the active device region to provide a control measurement aligned with the geometric centre of the device.

2.2 Sea conditions

The experimental setup considered within this study encompasses five distinct sea states, as outlined in Table 1. The first three sea states (SS1, SS2 and SS3) represent operational conditions from the North sea, scaled according to the prototype dimensions (see the discussion in Ringwood et al. 2023a). These are generated using a JONSWAP stochastic model (Hasselmann et al. 1973), defined by parameters such as peak period, significant wave height, and the peak-enhancement factor γ . In contrast, the remaining two conditions, WN1 and WN2, simulate 'white-noise' waves, characterised by a constant spectral density within a pre-defined frequency range. These have been specifically designed in Faedo et al. (2023a) for system identification purposes, enabling excitation of the prototype across its entire operational spectrum. Furthermore, for SS1 and SS3, two separate realisations (#R) are included to enrich the dataset available for training and validation.



For each wave condition outlined in Table 1, the following variables are recorded:

- θ : Angular position of the device relative to point **A**.
- $\dot{\theta}$: Angular velocity of the device relative to point A.
- $\ddot{\theta}$: Angular acceleration of the device relative to point **A**.
- *d*: Wave excitation torque induced by the free-surface elevation about point **A**. Note that this is, effectively, the variable to be estimated within Sect. 3.
- η_i : Free-surface elevation measured by wave probe i, where $i \in \mathbb{N}_7$.

The angular position and acceleration have been directly measured using the device's sensors in free-motion within the tank, for each corresponding sea-state condition. The angular velocity, on the other hand, has been derived from these measurements using standard sensor fusion techniques. In contrast, the wave excitation torque has been derived by mechanically locking the device and recording the total forces exerted using a dedicated load cell (see Fig. 1). For further details about the experimental setup, the reader is referred to Faedo et al. (2023a).

3 Data-based estimation of wave excitation

This section outlines the proposed methodology for estimating the wave-induced torque d, as described in Sect. 2.3, employing tailored data-based techniques. The subsequent paragraphs detail the process of input variable selection, an overview of the NN architectures utilised, and the design of the training and testing frameworks based on the experimental setup and corresponding data presented in Sect. 2.

Note that none of the steps involved within the proposed data-based estimators, detailed below, depend explicitly on the scale of the device being considered. That is, the data measured and used for training and validation of the estimators is derived from standard instrumentation (wave gauges and motion sensors, as detailed within Sect. 2.1), which are widely available for any realistic device scale. This is, in fact, a significant advantage of the proposed data-based estimators when compared with their model-based counterparts, which commonly employ models derived from black-box system identification procedures Papini et al. (2024), being hence difficult to scale consistently.

3.1 Input feature selection

In data-based estimation approaches, the relevance of input features is critical to ensuring accurate and robust NN estimator performance. To ensure that the selected inputs provide



Table 1 Waves used for training and validation of the proposed data-based estimators for wave excitation torque

ID	Туре	Period (s)	Height (m)	γ	#R	Length (s)
SS1	Operational	1.412	0.063	3.3	2	300
SS2	Operational	1.836	0.104	3.3	1	300
SS3	Operational	0.988	0.021	1	2	300
WN1	Identification	[0.5, 10]	0.03	_	1	300
WN2	Identification	[0.5, 10]	0.05	-	1	300

meaningful information for estimating the target signal d, a comprehensive input feature selection process is conducted from two complementary perspectives: correlation and frequency-domain analysis based on spectral coherence.

It is worth noting that the presented analysis is carried out using the entire available dataset detailed in Sect. 2, ensuring a comprehensive and statistically representative evaluation of the collected information.

1. Correlation analysis A Spearman correlation analysis is performed to evaluate the monotonic relationships between potential input variables and the target signal *d*. This non-parametric method provides insights into both linear and non-linear associations, enabling the identification of variables with strong predictive potential. Although correlation does not imply causation, it serves as an initial indicator of the potential importance of each feature in establishing relationships with the target signal.

Table 2 presents the Spearman correlation coefficients calculated between the system variables including, angular position θ , angular velocity $\dot{\theta}$, angular acceleration $\ddot{\theta}$, and surrounding wave height measurements η_i with respect to the target variable d. It is worth mentioning that a positive correlation coefficient indicates that two variables tend to increase or decrease simultaneously, while a negative coefficient suggests an inverse relationship. Notably, θ exhibits a relatively strong positive correlation with d, with a coefficient of 0.613, underscoring its relevance in capturing the dynamic behaviour of the WEC. In contrast, $\dot{\theta}$ and $\ddot{\theta}$ show a weaker correlation (0.253 and -0.268), likely due to the lag introduced by the system dynamics. Among the wave height measurements, η_4 , η_5 and η_7 demonstrate strong negative correlations, with coefficients of -0.860, -0.856, and -0.819, respectively.

2. Frequency-domain analysis To complement the correlation-based evaluation, a spectral coherence analysis is conducted to quantify the linear relationship between signals in the frequency domain. Coherency Spectrum (squared magnitude), denoted as $C_{xy}(f)$, measures the normalised cross-spectral density between two signals x(t) and y(t) at each frequency f, and is defined as (Stoica et al. 2005):

$$C_{xy}(f) = \frac{|P_{xy}(f)|^2}{P_{xx}(f)P_{yy}(f)},\tag{1}$$

where $P_{xy}(f)$ is the cross-spectral density between x(t) and y(t) and $P_{xx}(f)$ and $P_{yy}(f)$ are the power spectral densities of x(t) and y(t), respectively. The coherence values range from 0 to 1, with higher values indicating a stronger linear relationship between the signals at a given frequency.

Figure 3 presents the results of the spectral coherence analysis, with the left plot showing the coherence between motion variables $(\theta, \dot{\theta} \text{ and } \ddot{\theta})$ and the target variable d, and the right side displaying the coherence for wave height measurements $(\eta_i, i \in \mathbb{N}_7)$ with respect to d. These plots serve as a graphical method to assess the linear relationship between the signals across the frequency spectrum. A higher area under the coherence curve (AUC) indicates a stronger linear correlation over a broader frequency band. The analysis is conducted within the frequency range of 0.3-2.25 Hz, which corresponds to the bandwidth of interest for the WEC device. This range is determined based on the operational dynamics of the system, as it encompasses the dominant frequency content associated with the device's response to wave excitation. For instance, in SS2, the lower bound of 0.3 Hz (approximately 2 rad/s) represents the slowest significant oscillatory behaviour of the device, while the upper bound of 2.25 Hz (14 rad/s) captures the highest frequency dynamics relevant to the system's operation, as reported in Faedo et al. (2023a). To systematically evaluate the relevance of each input variable, the normalized spectral coherence AUC is computed within this frequency range, ensuring that the analysis focuses on the most significant dynamics of d for device operation. Table 3 summarises the normalised AUC values for each input variable, providing a quantitative basis for input selection Within this frequency range, wave height measurements η_4 and η_5 exhibit the strongest coherence with d, followed by the motion variables θ , $\dot{\theta}$ and $\ddot{\theta}$. This coherence analysis suggests that these signals capture critical information about the wave excitation dynamics, particularly in the frequency bands where d exhibits its highest energy.

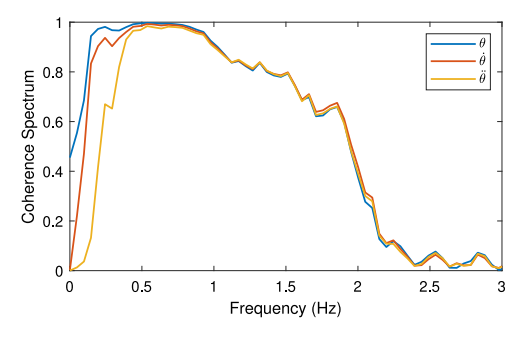
3.2 Neural network architectures

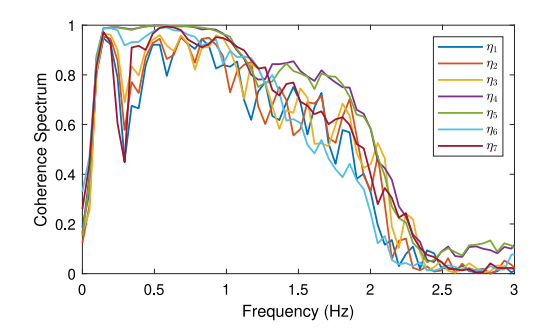
Five distinct NN architectures are implemented to evaluate their performance in reconstructing the target variable d. These architectures are described below:



Table 2 Spearman correlation coefficients of the variables with respect to the target variable d

Variable	θ	$\dot{ heta}$	$\ddot{ heta}$	η_1	η_2	η_3	η_4	η_5	η_6	η_7
Spearman coefficient	0.613	0.253	-0.268	0.220	0.150	0.046	-0.860	-0.856	-0.279	-0.819





- (a) Coherence between kinematic variables $(\theta, \dot{\theta}, \text{ and } \ddot{\theta})$ and the target variable d.
- (b) Coherence for wave height measurements $(\eta_1, \eta_2, \text{ etc.})$ with respect to d.

Fig. 3 Results of the spectral coherence analysis

Table 3 Normalized spectral coherence area values of the input variables with respect to the target variable d

Variable	θ	$\dot{ heta}$	$\ddot{ heta}$	η_1	η_2	η_3	η_4	η_5	η_6	η_7
Spectral coherence AUC	0.750	0.756	0.745	0.648	0.682	0.702	0.810	0.800	0.664	0.740

Feedforward neural network (FNN): a classical static NN designed to model relationships between input and output variables. This architecture consists of one hidden layer with 8 neurons with hyperbolic tangent (tanh) as a non-linear activation function. The output layer is fully connected with a linear activation function for regression tasks. The choice of the tanh activation function is based on its effectiveness in regression tasks involving single-layer NNs, as it provides smooth gradients and bounded outputs, which help stabilise training and mitigate saturation issues in shallow networks (Szandała 2020). The mathematical representation of a fully connected layer is given by:

$$y = \mathcal{H}(W^{\top}U + b), \tag{2}$$

where U is the input vector, W is the weight matrix, b is the bias term and \mathcal{H} denotes the activation function.

FNN_{big}: an extended version of the FNN with increased depth to capture more complex patterns. It consists of 8 hidden layers, each with 8 neurons, and uses the same tanh activation function. The output layer remains fully connected with a linear activation function.

Time delay neural network (TDNN): a FNN specifically designed to incorporate temporal information by including past samples of the input signals. This architecture is similar to the classical FNN, featuring one hidden layer with 8 neurons and one output layer, but extends its input by con-

sidering up to 7 past samples of each input signal. Although this modification increases the number of weights per neuron in the hidden layer, it allows the model to explicitly capture certain temporary dependencies in the data. In particular, the number of past samples is determined through a sensitivity analysis conducted using Bayesian optimization. This analysis systematically evaluates the impact of varying the number of past samples on the estimation performance, revealing that the chosen configuration provides a suitable trade-off between the complexity introduced to the network and the accuracy achieved.

Recurrent neural network (RNN): this type of NN incorporates feedback connections, enabling it to maintain an internal state per neuron that acts as a form of memory over time. This characteristic makes RNNs particularly well-suited for modelling sequential data and capturing temporal dependencies. In this paper, the RNN architecture consists of one recurrent layer containing 8 neurons and a linear fully connected layer as output. The equations governing the RNN with a single hidden layer are as follows:

$$h_k = \mathcal{H}(W_{uh}u_k + W_{hh}h_{k-1} + b_h),$$

$$y_k = W_{hy}h_k + b_y,$$
(3)

where u_k represents the input at time step k, which corresponds to samples of input signals. The term h_k denotes the hidden state of the neurons in the recurrent layer. The output



of the RNN, denoted by y_k , is computed as a linear transformation of the hidden state. In these equations, W_{uh} , W_{hh} and W_{hy} are weight matrices, and b_h and b_y are bias terms which are obtained during the training process. Additionally, \mathcal{H} represents a non-linear activation function applied to introduce non-linearity into the model, in this case, again tanh.

Long short-term memory (LSTM): these networks incorporate a sophisticated structure with multiple internal states, including a memory cell that can retain information over extended periods. This is achieved through gating mechanisms that regulate the flow of information at short and long terms. The architecture used in this work consists of one recurrent layer with 8 LSTM cells, each maintaining two internal states, followed by a linear fully connected output layer. The governing equations for an LSTM cell are as follows:

Input gate:
$$i_k = \sigma(W_i u_k + V_i h_{k-1} + b_i)$$
. (4)

Forget gate:
$$f_k = \sigma(W_f u_k + V_f h_{k-1} + b_f)$$
. (5)

Output gate:
$$o_k = \sigma(W_o u_k + V_o h_{k-1} + b_o)$$
. (6)

Cell state:
$$c_k = f_k \odot c_{k-1}$$

$$+i_k \odot \tanh(W_c u_k + V_c h_{k-1} + b_c).$$
 (7)

Hidden state:
$$h_k = o_k \odot \tanh(c_k)$$
. (8)

Cell output:
$$y_k = h_k$$
, (9)

where u_k is the input at time step k, h_{k-1} and c_{k-1} are the hidden state and cell state at the previous time step, W_i , W_f , W_c , and W_o are the weight matrices for the input, forget, cell and output gates, respectively. V_i , V_f , V_c and V_o are the recurrent weight matrices, b_i , b_f , b_c and b_o are bias vectors, σ is the sigmoid activation, and \odot denotes the standard Hadamard product (element-wise multiplication).

Although a wide range of neural network configurations could be explored, the architectures selected are designed to balance computational complexity with the inherent dynamics of the WEC system. As described earlier, static architectures such as FNN, FNNbig and TDNN perform a direct, time-invariant mapping of inputs to outputs without incorporating explicit dynamic structures. In these NN, the temporal dynamics of the system are implicitly captured through the behaviour of the input variables themselves, effectively delegating the representation of dynamic effects to these variables. In contrast, recurrent architectures, like RNN and LSTM, explicitly model temporal dependencies through internal states, with each recurrent cell maintaining one and two non-linear dynamic states, respectively. This distinction highlights the trade-offs between static and dynamic modelling approaches, particularly in terms of complexity and their ability to capture temporal dependencies. The use of a single hidden layer is motivated by its empirical effectiveness in preliminary tests, which showed that deeper networks provided only marginal performance gains while increasing training complexity. This design choice aligns with previous applications in renewable energy systems, where shallow architectures have demonstrated sufficient accuracy and generalisation capability in estimating physical variables (Bimenyimana et al. 2017; Saavedra et al. 2024). All architectures considered in this work share this same neural structure (i.e. one hidden layer with 8 neurons), ensuring a fair comparison across different network types.

The specific choice of 8 neurons is motivated by both physical and computational considerations. From a modelling perspective, the authors of Pasta et al. (2024) consider a 6thorder dynamical model to approximate the linear behaviour of the device, suggesting that at least 6 internal states may be necessary to effectively characterise the system dynamics. While the current work focuses on the inverse dynamic problem, in the context of dynamic NNs such as RNNs, where each neuron may represent a hidden state as described by (3), a comparable number of recurrent units would be required to capture this dimensionality. Nonetheless, additional neurons are included to enhance approximation accuracy and minimise output error. From a computational standpoint, as discussed in Livni et al. (2014), selecting a number of neurons that is a power of two facilitates faster convergence due to hardware-level optimisations and improved memory access efficiency. Consequently, 8 neurons are chosen as the closest power of two greater than 6, ensuring both sufficient representational capacity and efficient training. Although different configurations (e.g. 4, 16, 32 neurons) were experimentally evaluated, the performance gains obtained with larger neuron counts do not justify the increased computational burden. This is particularly evident in complex recurrent models such as LSTM. Therefore, the choice of 8 neurons represents a balanced and fair configuration across architectures for comparative purposes.

3.3 Training and testing scheme

To train and validate the neural estimators, the dataset is structured as follows. First, the experimental data is grouped according to operational sea state conditions (SS1, SS2, SS3) and the identification dataset (WN), which includes the wave conditions WN1 and WN2 (see Table 1). Each of these four groups is then split into two subsets: 70% of the data is used for training the NN models, while the remaining 30% is reserved for validation to assess the models' generalisation capabilities. This partitioning ensures a robust evaluation of performance across all sea state conditions.

In order to systematically evaluate the impact of input configurations on estimation performance, four distinct groups of NN architectures are defined based on their input features. The first group ($Group\ NNI$) is trained using angular position θ and angular velocity $\dot{\theta}$ as inputs. This selection is motivated



by the observation that θ exhibits both a relatively strong positive Spearman correlation and high spectral coherence with respect to d. Additionally, $\dot{\theta}$ is included to capture the dynamic motion of the WEC device, thereby providing complementary frequency-domain information that enhances the characterisation of motion represented by θ . Notably, this input configuration aligns directly with the variable used by the benchmark KBF, which relies solely on θ , ensuring a fair comparative evaluation. However, as discussed in Sect. 2.3, velocity is not directly measured by the WEC's instrumentation but is instead derived from available measurements using standard sensor fusion techniques. In response to this limitation, an alternative input configuration is explored, utilising variables directly measured by the WEC's instrumentation: position θ and acceleration $\ddot{\theta}$. This second group of neural networks is referred to as Group NN2.

Further developing on input configurations, the third group (*Group NN3*) extends *Group NN2* by incorporating surrounding wave height measurements (η_4 , η_5 and η_7). As demonstrated in Sect. 3.1, these signals exhibit strong negative correlations with d and high spectral coherence within the dominant frequency range of d. By incorporating spatial information about the wave, *Group NN3* addresses the potential limitations of WEC motion variables. Finally, a fourth group (*Group NN4*) is introduced, which comprises θ , $\dot{\theta}$ and $\ddot{\theta}$ as inputs. This configuration explores the feasibility of relying exclusively on variables related to the WEC's motion, avoiding the need for additional instrumentation while maintaining a comprehensive representation of the system dynamics.

The training process for static NNs utilises the Levenberg–Marquardt algorithm, which is particularly effective in converging to a solution in few iterations, even in the presence of multiple local minima (Marquardt 1963). This optimization method combines the strengths of gradient descent and the Gauss-Newton approach, providing improved computational stability and performance. For recurrent architectures such as RNN and LSTM, the training process incorporates Backpropagation Through Time (BPTT) (Werbos 1990), which is essential for effectively capturing temporal dependencies in sequential data. The objective of the optimization is to minimise the Mean Square Error (MSE), which serves as the cost function, by iteratively adjusting the synaptic weights of the networks.

To ensure the proper functioning of the RNN and LSTM models, special attention is given to the temporal dynamics of the system. Since these architectures inherently rely on temporal patterns, the dataset is subjected to a preprocessing step involving downsampling from 200 to 50 Hz. This adjustment not only provides a broader perspective on the changes in system behaviour with fewer samples but also satisfies the Nyquist–Shannon sampling theorem with significant margin, as the frequency band of interest lies below 2.25 Hz.

Additionally, a low-pass fourth-order Butterworth digital filter is applied to the $\ddot{\theta}$ signal to mitigate high-frequency noise components. This preprocessing step ensures that the essential dynamics of the system are preserved while minimising the impact of potential noise sources. Furthermore, the input variables for all four groups of NN are normalized using the min-max scaling method, ensuring all features are rescaled to a comparable range between 0 and 1. This preprocessing mitigates numerical issues such as gradient explosions or vanishing gradients during training and ensures that all input features are on a consistent scale, further enhancing the stability and efficiency of the learning process.

4 Results

This section presents the results of the NN-based wave excitation force estimators described in Sect. 3. The performance analysis focuses on comparing static architectures with those incorporating temporal dynamics, across the four NN groups and under varying sea state conditions. For comparative purposes, a KBF with HO extension, experimentally tuned in Papini et al. (2024), is utilised as a benchmark. Comprehensive details regarding its theoretical formulation, parameter tuning, and validation are extensively documented in the referenced work. Note that, as per Papini et al. (2024), the tuning of the KBF has been done taking into account all operational sea-states considered (see Sect. 2.2). This creates a level playing field for comparison with the proposed databased observers, which are also tuned taking into account all the considered operating conditions, and not just tuned individually for each tank test.

The performance metrics for the NN-based estimators are summarised in Tables 4, 5, 6, and 7, corresponding to *Groups NN1*, *NN2*, *NN3*, and *NN4*, respectively. Each table also includes the results of the KBF benchmark for comparative evaluation. These tables present the performance across different sea states (SS1, SS2, SS3), the identification dataset (WN), and the averaged whole figure. The evaluation metrics comprise the MSE, Mean Absolute Error (MAE), and Coefficient of Determination (R^2), providing a comprehensive assessment of each model's capability in estimating wave-induced torque. Specifically, MSE and MAE quantify estimation errors, while R^2 evaluates the proportion of variance in the target variable explained by the model.

In Table 4 (*Group NN1*), static neural networks (FNN and FNN_{big}) exhibit significant limitations, with consistently higher MSE and MAE values compared to the KBF across most sea states. For instance, in SS2, the FNN achieves an MSE of 3.740, nearly double the KBF's 1.830. However, architectures incorporating temporal considerations (TDNN, RNN, and LSTM) demonstrate marked improvements. Notably, the TDNN achieves the lowest MSE (0.088)



Table 4 Comparison of performance metrics for *Group NN1* (θ and $\dot{\theta}$ as inputs)

Metric	Model	Dataset				
		SS1	SS2	SS3	WN	Complete
MSE	KBF	0.451	1.830	0.249	1.474	1.001
	FNN	1.560	3.740	0.437	2.250	1.997
	FNN_{big}	1.556	3.722	0.434	2.245	1.989
	TDNN	0.088	0.200	0.098	0.129	0.129
	RNN	0.114	0.221	0.131	0.171	0.159
	LSTM	0.270	0.569	0.315	0.384	0.385
MAE	KBF	0.516	0.841	0.396	0.965	0.679
	FNN	1.009	1.557	0.523	1.198	1.072
	FNN_{big}	1.006	1.554	0.522	1.194	1.069
	TDNN	0.226	0.346	0.245	0.280	0.274
	RNN	0.267	0.363	0.284	0.320	0.308
	LSTM	0.409	0.598	0.409	0.478	0.474
R^2	KBF	0.909	0.886	0.472	0.564	0.708
	FNN	0.685	0.765	0.074	0.334	0.465
	FNN_{big}	0.686	0.766	0.080	0.336	0.467
	TDNN	0.982	0.987	0.793	0.962	0.931
	RNN	0.977	0.986	0.723	0.949	0.909
	LSTM	0.946	0.964	0.332	0.886	0.782

Bold values highlight the minimum value for each column

Table 5 Comparison of performance metrics for *Group NN2* (θ and $\ddot{\theta}$ as inputs)

Metric	Model	Dataset							
		SS1	SS2	SS3	WN	Complete			
MSE	KBF	0.451	1.830	0.249	1.474	1.001			
	FNN	0.643	1.000	0.341	0.802	0.697			
	FNN_{big}	0.643	1.013	0.339	0.802	0.699			
	TDNN	0.097	0.215	0.065	0.103	0.120			
	RNN	0.136	0.731	0.073	0.118	0.264			
	LSTM	0.148	0.349	0.103	0.140	0.185			
MAE	KBF	0.516	0.841	0.396	0.965	0.679			
	FNN	0.645	0.789	0.486	0.702	0.656			
	FNN_{big}	0.645	0.796	0.485	0.702	0.657			
	TDNN	0.238	0.357	0.205	0.245	0.261			
	RNN	0.269	0.391	0.220	0.241	0.280			
	LSTM	0.301	0.446	0.258	0.292	0.324			
R^2	KBF	0.909	0.886	0.472	0.564	0.708			
	FNN	0.870	0.937	0.277	0.763	0.712			
	FNN_{big}	0.870	0.936	0.282	0.763	0.713			
	TDNN	0.980	0.986	0.863	0.970	0.950			
	RNN	0.973	0.954	0.844	0.965	0.934			
	LSTM	0.970	0.978	0.781	0.959	0.922			

Bold values highlight the minimum value for each column

Table 6 Comparison of performance metrics for *Group NN3* (θ , $\ddot{\theta}$, η_4 , η_5 and η_7 as inputs)

Metric	Model	Dataset	;			
		SS1	SS2	SS3	WN	Complete
MSE	KBF	0.451	1.830	0.249	1.474	1.001
	FNN	0.325	0.919	0.200	0.453	0.474
	FNN_{big}	0.323	0.911	0.195	0.457	0.471
	TDNN	0.089	0.154	0.088	0.097	0.107
	RNN	0.102	0.149	0.061	0.076	0.097
	LSTM	0.135	0.275	0.105	0.129	0.161
MAE	KBF	0.516	0.841	0.396	0.965	0.679
	FNN	0.447	0.733	0.367	0.529	0.519
	FNN_{big}	0.445	0.725	0.362	0.531	0.515
	TDNN	0.226	0.295	0.241	0.238	0.250
	RNN	0.243	0.295	0.197	0.213	0.237
	LSTM	0.283	0.403	0.261	0.281	0.294
R^2	KBF	0.909	0.886	0.472	0.564	0.708
	FNN	0.934	0.942	0.575	0.866	0.829
	FNN_{big}	0.935	0.943	0.587	0.865	0.833
	TDNN	0.982	0.990	0.814	0.971	0.939
	RNN	0.979	0.991	0.871	0.978	0.955
	LSTM	0.973	0.983	0.777	0.962	0.924

Bold values highlight the minimum value for each column

Table 7 Comparison of performance metrics for *Group NN4* $(\theta, \dot{\theta})$ and $\ddot{\theta}$ as inputs)

Metric	Model	Dataset				
		SS1	SS2	SS3	WN	Complete
MSE	KBF	0.451	1.830	0.249	1.474	1.001
	FNN	0.379	0.492	0.067	0.232	0.293
	FNN_{big}	0.374	0.502	0.059	0.234	0.292
	TDNN	0.096	0.213	0.061	0.086	0.114
	RNN	0.104	0.203	0.054	0.078	0.110
	LSTM	0.139	0.273	0.086	0.116	0.153
MAE	KBF	0.516	0.841	0.396	0.965	0.679
	FNN	0.478	0.558	0.200	0.379	0.404
	FNN_{big}	0.475	0.561	0.190	0.378	0.401
	TDNN	0.239	0.359	0.196	0.228	0.255
	RNN	0.247	0.347	0.181	0.219	0.248
	LSTM	0.288	0.408	0.236	0.266	0.299
R^2	KBF	0.909	0.886	0.472	0.564	0.708
	FNN	0.924	0.969	0.857	0.931	0.920
	FNN_{big}	0.925	0.969	0.875	0.931	0.925
	TDNN	0.981	0.987	0.872	0.975	0.953
	RNN	0.979	0.987	0.886	0.977	0.957
	LSTM	0.972	0.983	0.818	0.966	0.935

Bold values highlight the minimum value for each column



in SS1, 0.200 in SS2 and 0.129 in WN) and highest R^2 (0.982 in SS1, 0.987 in SS2 and 0.962 in WN), outperforming the KBF by 80.5% MSE reduction in SS1 89.1% in SS2 and 91.2% in WN. SS3 is the most challenging scenario due to its wide-banded power spectral density, covering virtually all the operation space for the considered prototype, as previously reported in Papini et al. (2024). This characteristic poses significant estimation challenges for the KBF achieving an R^2 of 0.472 in this condition. In contrast, the TDNN demonstrates a better performance, achieving an R^2 of 0.793.

Group NN2 (Table 5) replaces $\dot{\theta}$ with $\ddot{\theta}$ as the second input, alongside θ . Static networks, despite exhibiting considerable errors compared to networks with temporal considerations, achieve performance comparable to the KBF in SS1 and SS2. Specifically, the static networks attain R^2 values of 0.87 and 0.93 in SS1 and SS2, respectively, which are close to the KBF's R^2 values of 0.909 and 0.886. However, their performance in SS3 remains lower, with R^2 values of 0.277 and 0.282 for FNN and FNN_{big}, respectively, highlighting a persistent challenge in capturing the variability of d. Once again, the TDNN stands out as the top performer, followed closely by the RNN. This suggests that $\ddot{\theta}$ provides similar information to velocity $\dot{\theta}$ when combined with θ for recurrent and with past samples as input architectures, obtaining almost the same values for SS1 and SS2 while slightly improving performance for SS3 and WN.

The incorporation of surrounding wave height measurements $(\eta_4, \eta_5, \text{ and } \eta_7)$ in *Group NN3* (see Table 6) results in a significant improvement in estimation accuracy, particularly for static NN architectures. These estimators benefit substantially from the additional inputs, outperforming the KBF even in challenging conditions such as SS3, with MSE values of 0.474 and 0.471 in the complete dataset, respectively, compared to the KBF's 1.001. It is important to note, however, that the KBF does not leverage wave height information, which may partly explain its comparatively lower performance. Meanwhile, networks incorporating temporal dynamics maintain their dominance, with TDNN and RNN achieving the lowest errors overall. However, these models do not exhibit significantly greater improvements relative to their performance in previous input groups. Notably, the RNN achieves the best results within this group, with an MSE value of 0.097 in the complete dataset, surpassing all other models.

Despite omitting wave height measurements, *Group NN4* (see Table 7) achieves performance metrics comparable to those of *NN3*. This suggests that the inclusion of velocity complements acceleration and position like the surrounding height measurements. Comparing *NN4* with *NN2*, the former gets a better performance for the static networks with similar results for recurrent ones. For instance, the RNN achieves an R^2 value of 0.957 in the overall dataset, closely aligning with the 0.955 observed in *Group NN3* and the 0.950 achieved

in *Group NN2*. Similarly, the TDNN and LSTM maintain strong performance, achieving R^2 values of 0.953 and 0.935, respectively.

5 Discussion

The findings presented in Sect. 4 highlight the impact of input feature selection on the performance of NN-based estimators for wave excitation effects, particularly in static models. Both the inclusion of surrounding wave height measurements in Group NN3 models and the use of all three device motion signals lead to improved estimation accuracy in static models compared to those relying solely on θ and $\dot{\theta}$ or θ and $\ddot{\theta}$. This improvement is especially evident in challenging sea states such as SS3, where the presence of additional signals reduces the MSE. However, while wave height measurements provide valuable information, their integration introduces practical challenges. These measurements require additional instrumentation for the WEC, increasing system complexity and overall capital costs. Moreover, reliance on external sensors for wave height data may introduce uncertainties due to sensor placement and calibration errors. From a practical standpoint, the use of neural networks with temporal considerations from Group NN2 offers several advantages. The variables used as inputs in this group are directly measured by standard WEC instrumentation, eliminating the need for additional sensors and thereby reducing implementation costs. Furthermore, this approach avoids the need for sensor fusion strategies to derive the $\dot{\theta}$ signal. Despite using only two input variables (θ and $\ddot{\theta}$), these estimators achieve performance metrics that are only marginally inferior to those of Group NN3 and Group NN4, suggesting a better practical effectiveness. Additionally, this approach simplifies data acquisition and processing pipelines, enhancing the robustness of the estimation framework. While wave height measurements or the $\dot{\theta}$ signal remain valuable for certain applications, their substitution with measurement-based inputs represents a cost-effective alternative almost without compromising performance.

Regarding the type of neural network, the static networks (FNN and FNN_{big}) show limited competitiveness, with performance varying significantly depending on the input configuration. The TDNN and RNN consistently emerge as the top-performing architectures across the considered input groups. The RNN demonstrates superior performance when additional input signals to WEC motion measurements are available (*Group NN3* and *Group NN4*). In contrast, the TDNN stands out in scenarios with fewer inputs (*Group NN1* and *Group NN2*), particularly within *Group NN2*, as discussed above. The LSTM ranks third, offering moderate improvements over static models, but falling short of simpler recurrent architectures in this application, likely due to the



signal's lack of long-term dependencies, as discussed in the following paragraph. Overall, the obtained results highlight the critical role of temporal considerations and, in a second stage, supplementary input features.

Despite the theoretical advantages of LSTM networks in capturing long-term dependencies, the results indicate that, in this problem, these architectures do not outperform simpler recurrent models such as RNN or even static architectures incorporating past samples, like TDNN. Using the Augmented Dickey-Fuller (ADF) (Dickey and Fuller 1979) and Kwiatkowski-Phillips-Schmidt-Shin (KPSS) (Kwiatkowski et al. 1992) tests results that the signal to be estimated is stationary over time across all sea states. Consequently, it is possible to analyse the temporal characteristics of the signal using the Hurst exponent (H) via Rescaled Range (R/S)analysis (Hurst 1951). The Hurst exponent quantifies the persistence or anti-persistence of a time series, with H > 0.5indicating long-term memory, H < 0.5 suggesting antipersistence, and H = 0.5 reflecting random behaviour. In this case, the calculated Hurst exponents for d across different sea states are as follows: H = 0.36 for SS1, H = 0.27for SS2 and H = 0.48 for SS3 and H = 0.21 for the identification dataset WN. These values reveal predominantly anti-persistent behaviour in SS1, SS2 and WN, where trends tend to reverse over time due to their predominantly sinusoidal nature. Notably, SS3 exhibits near-random behaviour $(H \approx 0.5)$, indicating a lack of significant temporal structure. This aligns with its wide-banded spectral characteristics, which introduce rapid and unpredictable variations in the signal, implying that d lacks long-term temporal dependencies. Consequently, the sophisticated long-term memory mechanisms of LSTMs may introduce unnecessary complexity and noise into the estimation process. In contrast, simpler architectures such as RNNs and TDNNs (even with fixed short-term input windows) are sufficient to capture the oscillatory and anti-persistent temporal dependencies of the signal d, with reduced computational overhead. This is further supported by prior studies demonstrating that RNNs can outperform LSTMs in tasks dominated by short-term dynamics (Zhao et al. 2020; Saavedra et al. 2024; Abdulkarim and Engelbrecht 2019).

Finally, the superior performance of NNs compared to the linear model-based estimator can be attributed to fundamental differences in their underlying principles. While the KBF relies on a linear model of the system dynamics (Papini et al. 2024), NNs inherently capture non-linear interactions through data-based mappings, enabling them to adapt to unmodelled hydrodynamic effects. To provide a visual validation of the proposed NN estimators, Fig. 4 presents representative temporal signals of wave-induced torque for each sea state. The figure compares three signals: the real measured torque (d), the KBF estimation ((\hat{d}_{KBF})), and the proposed TDNN ($Group\ NN2$) estimation ((\hat{d}_{TDNN})). This

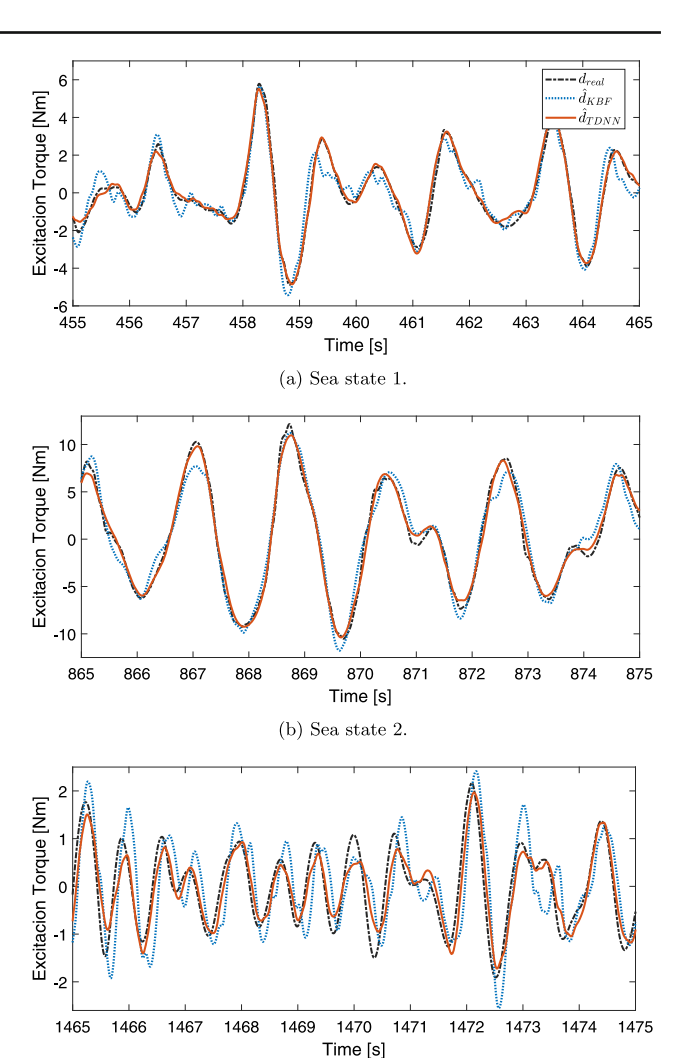


Fig. 4 Temporal wave-induced torque estimation across different sea states. Comparison between ground truth (black), KBF estimation (blue), and TDNN (*Group NN2*) estimation (orange) (colour figure online)

(c) Sea state 3.

graph focuses on the TDNN model, as it achieves the best trade-off between estimation performance, network complexity, and input measurement requirements compared to other models. For the estimations presented here, the signals from all operating three sea states are concatenated, with each plot (Fig. 4a–c) showing a 10-s snippet corresponding to ≈ 5 typical periods in the longer case (*i.e.*, SS2). These plots offer a qualitative assessment of the estimation performance across different maritime conditions.

The temporal signals in Fig. 4 corroborate the previously reported performance metrics, revealing distinct model behaviours across sea states. In SS1 and SS2, where conditions align more closely with the assumptions adopted when modelling the device dynamics within the KBF, both the KBF and TDNN demonstrate reliable accuracy. The TDNN, however, demonstrates the most accurate estimation

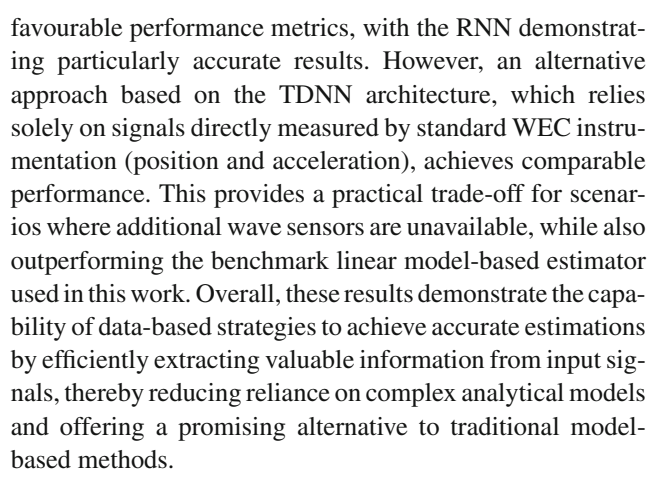


by closely tracking the ground truth with minimal deviation. Conversely, in SS3, the KBF exhibits significant limitations, likely due to unmodelled non-linear hydrodynamic effects that are more predominant in this case (see Fig. 4c). In contrast, the RNN demonstrates an enhanced capability in capturing complex wave-induced torque dynamics under these wide-banded and turbulent conditions.

Although the results demonstrate that the TDNN outperforms the KBF used as a benchmark in this work, it is important to note that the KBF represents a specific implementation within the broader class of linear model-based approaches. Alternative formulations, such as non-linear extensions or other observers, could yield different outcomes. Despite this, the findings underscore the potential of databased techniques to effectively handle non-linearities and uncertainties inherent in wave-induced torque estimation, offering a promising complement to traditional methodologies. Notably, while data-based estimators perform well with the current dataset, their accuracy depends heavily on the informativeness of the training data, which must adequately represent the range of possible wave conditions. In contrast to model-based approaches, data-based methods require less prior knowledge of system dynamics but rely extensively on large, high-quality datasets for training. Conversely, modelbased estimators depend significantly on accurate system modelling, which can limit their adaptability to new scenarios, often necessitating complex recalibration or even a complete redesign of the underlying model. On the other hand, data-based estimators can be updated by retraining offline with new data collected under the corresponding conditions. This ensures their continued relevance and effectiveness while maintaining a straightforward implementation process, without introducing additional computational complexity. Regarding the computational footprint, it is important to note that all significant computational effort is relegated to the offline training phase. Once the model is trained, the inference process using the estimator is computationally lightweight particularly for NN architectures without recurrent connections. This characteristic makes it feasible to deploy these trained neural models on resource-constrained platforms such as microcontrollers (Ray 2022; Estrebou et al. 2022) or Programmable Logic Controllers (PLCs) (Lai and Ma 2023), which are commonly used in industrial applications.

6 Conclusions and future work

The findings reveal that NN architectures incorporating temporal considerations achieve superior estimation performance compared to static NN estimators. The inclusion of surrounding wave height data or all three device motion-related variables enables these estimators to achieve the most



Future work will encompass two primary directions. First, the proposed approach will be experimentally validated using a real WEC prototype in a wave tank environment following the in-situ (online) validation proposed in Papini et al. (2024), ensuring its robustness and reliability under realistic operating conditions. Second, the integration of the estimator into the control loop will be explored to enhance system performance, enabling more adaptive and efficient energy capture strategies. In addition, future works could explore the use of more advanced architectures, such as attentionbased models or convolutional-recurrent hybrids, to assess whether further performance gains can be achieved. Additionally, given the quasi-periodic nature of ocean waves, the proposed estimation framework could be extended to prediction tasks, enabling predictive or adaptive control strategies. These advancements have the potential to further optimise energy capture and contribute to the viability of wave energy technology.

Author Contributions All authors contributed to the study conception and design. Methodology, investigation, validation, formal analysis and visualisation were performed by MDS. Data curation was performed by NF and FDM. Supervision and funding acquisition were provided by NF, FAI and FG. The first draft of the manuscript was written by MDS, and review and editing were carried out by NF, FAI, FDM and FG. All authors read and approved the final manuscript.

Funding Open access funding provided by Politecnico di Torino within the CRUI-CARE Agreement. This research was funded by the Universidad Nacional de UNLP (Project I284, 11/I255), CONICET (PIP 112-2020-01-00331, PIP 112-2020-010281) y ANPCyT (PICT 2022-11-00352, PICT 3747). Project funded by the European Union - NextGenerationEU under the National Recovery and Resilience Plan (NRRP), Mission 4 Component 2 Investment 1.2 | Project code: MSCA2024_0000032—CUP: E13C25001010006—Project title: Unlocking wave power: Economic-aware control co-design for wave energy conversion (ECOWAVE).

Data availability No datasets were generated or analysed during the current study.

Declarations



Conflict of interest The authors declare no conflict of interest.

Open Access This article is licensed under a Creative Commons Attribution 4.0 International License, which permits use, sharing, adaptation, distribution and reproduction in any medium or format, as long as you give appropriate credit to the original author(s) and the source, provide a link to the Creative Commons licence, and indicate if changes were made. The images or other third party material in this article are included in the article's Creative Commons licence, unless indicated otherwise in a credit line to the material. If material is not included in the article's Creative Commons licence and your intended use is not permitted by statutory regulation or exceeds the permitted use, you will need to obtain permission directly from the copyright holder. To view a copy of this licence, visit http://creativecommons.org/licenses/by/4.0/.

References

- Abdulkarim SA, Engelbrecht AP (2019) Time series forecasting using neural networks: Are recurrent connections necessary? Neural Process Lett 50(3):2763–2795. https://doi.org/10.1007/s11063-019-10061-5
- Bimenyimana S, Asemota GNO, Lingling L (2017) Output power prediction of photovoltaic module using nonlinear autoregressive neural network. J Energy Environ Chem Eng 2(2):32–40. https:// doi.org/10.11648/j.jeece.20170202.13
- Bonfanti M, Carapellese F, Sirigu S, Bracco G, Mattiazzo G (2020a) Excitation forces estimation for non-linear wave energy converters: A neural network approach. IFAC-PapersOnLine 53(2):12334–1233 (21st IFAC World Congress). https://doi.org/ 10.1016/j.ifacol.2020.12.1213
- Bonfanti M, Hillis A, Sirigu SA, Dafnakis P, Bracco G, Mattiazzo G, Plummer AR (2020b) Real-time wave excitation forces estimation: an application on the ISWEC device. J Mar Sci Eng 8(10):825. https://doi.org/10.3390/jmse8100825
- Castro-Santos L, Garcia GP, Estanqueiro A, Justino PAPS (2015) The levelized cost of energy (LCOE) of wave energy using GIS based analysis: the case study of Portugal. Int J Electr Power Energy Syst 65:21–25. https://doi.org/10.1016/j.jiepes.2014.09.022
- Celesti ML, Papini G, Pasta E, Peña-Sanchez Y, Mosquera FD, Ferri F, Faedo N (2025) Experimental investigation of wave-to-force modelling uncertainty for wave energy converters. Mech Syst Signal Process 226:112323. https://doi.org/10.1016/j.ymssp.2025. 112323
- Chen WH, Yang J, Guo L, Li S (2015) Disturbance-observer-based control and related methods—an overview. IEEE Trans Ind Electron 63(2):1083–1095. https://doi.org/10.1109/TIE.2015.2478397
- Dickey DA, Fuller WA (1979) Distribution of the estimators for autoregressive time series with a unit root. J Am Stat Assoc 74(366):427–431. https://doi.org/10.1080/01621459.1979.10482531
- Estrebou CA, Fleming M, Saavedra MD, Adra F, De Giusti A (2022) Lightweight convolutional neural networks framework for really small TinyML devices. In: Narváez FR, Vallejo DF, Morillo P, Proaño J (eds) Smart technologies, systems and applications. Springer International Publishing, Cham, pp 3–16
- Faedo N, Bussi U, Peña-Sanchez Y, Windt C, Ringwood JV (2021) A simple and effective excitation force estimator for wave energy systems. IEEE Trans Sustain Energy 13(1):241–250. https://doi. org/10.1109/TSTE.2021.3108576
- Faedo N, Mattiazzo G, Ringwood JV (2022) Robust energy-maximising control of wave energy systems under input uncertainty. In: 2022 European control conference (ECC), London, pp 614–619. https:// doi.org/10.23919/ECC55457.2022.9838234

- Faedo N, Peña-Sanchez Y, Pasta E, Papini G, Mosquera FD, Ferri F (2023a) SWELL: an open-access experimental dataset for arrays of wave energy conversion systems. Renew Energy 212:699–716. https://doi.org/10.1016/j.renene.2023.05.069
- Faedo N, Peña-Sanchez Y, Pasta E, Papini G, Mosquera F, Ferri F (2023b) SWELL: an open-access experimental dataset for arrays of wave energy conversion systems. Mendeley Data. https://doi. org/10.17632/n34wcksmts.1
- Fornaro P, Mosquera FD, Puleston PF, Evangelista CA, Ringwood JV (2024) Homogeneous filtering unknown input observer for wave energy applications. In: 2024 IEEE 63rd conference on decision and control (CDC), Milan. IEEE, pp 4257–4426. https://doi.org/10.1109/CDC56724.2024.10886157
- Francis BA, Wonham WM (1976) The internal model principle of control theory. Automatica 12(5):457–465. https://doi.org/10.1016/0005-1098(76)90006-6
- Fusco F, Ringwood JV (2012) A simple and effective real-time controller for wave energy converters. IEEE Trans Sustain Energy 4(1):21–30
- García-Violini D, Faedo N, Peña-Sanchez Y, Nava V, Ringwood JV (2024) Revisiting excitation force estimation in WECs: on the (mis) use of structure-based estimation approaches. Ocean Eng 311:118864. https://doi.org/10.1016/j.oceaneng.2024.118864
- Gunn K, Stock-Williams C (2012) Quantifying the global wave power resource. Renew Energy 44:296–304. https://doi.org/10.1016/j. renene.2012.01.101
- Hansen RH, Kramer MM (2011) Modelling and control of the Wavestar prototype. In: 9th European wave and tidal energy conference (EWTEC), Southampton, pp 1–10
- Hasselmann K, Barnett TP, Bouws E, Carlson H, Cartwright DE, Enke K, Ewing JA, Gienapp H, Hasselmann DE, Kruseman P, Meerburg A, Miiller P, Olbers DJ, Richter K, Sell W, Walden H (1973)
 Measurements of wind-wave growth and swell decay during the joint north sea wave project (JONSWAP). Ergaenzungsheft zur Deutschen Hydrographischen Zeitschrift, Reihe A
- Hillis A, Brask A, Whitlam C (2020) Real-time wave excitation force estimation for an experimental multi-DOF WEC. Ocean Eng 213:107788. https://doi.org/10.1016/j.oceaneng.2020.107788
- Hurst HE (1951) Long-term storage capacity of reservoirs. Trans Am Soc Civ Eng 116:770–799. https://doi.org/10.1061/TACEAT. 0006518
- International Energy Agency (2021) Net zero by 2050: a roadmap for the global energy sector. https://www.iea.org/reports/net-zero-by-2050
- Kwiatkowski D, Phillips PC, Schmidt P, Shin Y (1992) Testing the null hypothesis of stationarity against the alternative of a unit root: how sure are we that economic time series have a unit root? J Econom 54(1–3):159–178
- Lai E, Ma J (2023) Intelligent uncertainty handling using artificial neural networks in a programmatic logic controller-based automation system. In: Proceedings of the ASME 2023 18th international manufacturing science and engineering conference, New Brunswick, V002T05A003. https://doi.org/10.1115/MSEC2023-101825
- Livni R, Shalev-Shwartz S, Shamir O (2014) On the computational efficiency of training neural networks. Adv Neural Inf Process Syst 27:1–9
- Mahmoodi K, Nepomuceno E, Razminia A (2022) Wave excitation force forecasting using neural networks. Energy 247:12332. https://doi.org/10.1016/j.energy.2022.123322
- Marquardt DW (1963) An algorithm for least-squares estimation of nonlinear parameters. J Soc Ind Appl Math 11(2):431–441
- Masoumi M, Estejab B, Henry F (2024) Implementation of machine learning techniques for the analysis of wave energy conversion systems: a comprehensive review. J Ocean Eng Mar Energy 10(3):641–670. https://doi.org/10.1007/s40722-024-00330-4



- Mosquera FD, Fornaro P, Puleston PF, Evangelista CA, Ringwood JV (2024) A sliding mode-based tracking observer for excitation force estimation in wave energy systems. In: 2024 IEEE conference on control technology and applications (CCTA), Newcastle upon Tyne. IEEE, pp 598–603. https://doi.org/10.1109/CCTA60707. 2024.10666656
- Nguyen HN, Tona P (2017) Wave excitation force estimation for wave energy converters of the point-absorber type. IEEE Trans Control Syst Technol 26(6):2173–2181. https://doi.org/10.1109/ TCST.2017.2747508
- Papini G, Pasta E, Peña-Sanchez Y, Mosquera FD, Garcia-Violini D, Ferri F, Faedo N (2024) Assessment and validation of wave excitation force estimators in operative conditions. Control Eng Pract 151:106019. https://doi.org/10.1016/j.conengprac.2024.106019
- Pasta E, Papini G, Peña-Sanchez Y, Mosquera FD, Ferri F, Faedo N (2024) Data-based modelling of arrays of wave energy systems: experimental tests, models, and validation. Control Eng Pract 148:105949. https://doi.org/10.1016/j.conengprac.2024.105949
- Peña-Sanchez Y, Windt C, Davidson J, Ringwood JV (2019) A critical comparison of excitation force estimators for wave-energy devices. IEEE Trans Control Syst Technol 28(6):2263–2275. https://doi. org/10.1109/TCST.2019.2939092
- Ray PP (2022) A review on TinyML: state-of-the-art and prospects. J King Saud Univ Comput Inf Sci 34(4):1595–1623. https://doi.org/10.1016/j.jksuci.2021.11.019
- Ringwood JV, Tom N, Ferri F, Yu Y-H, Coe RG, Ruehl K, Bacelli G, Shi S, Patton RJ, Tona P, Sabiron G, Merigaud A, Ling BA, Faedo N (2023a) The wave energy converter control competition (WECCCOMP): wave energy control algorithms compared in both simulation and tank testing. Appl Ocean Res 138:10365. https://doi.org/10.1016/j.apor.2023.103653
- Ringwood JV, Zhan S, Faedo N (2023b) Empowering wave energy with control technology: possibilities and pitfalls. Annu Rev Control 55:18–44. https://doi.org/10.1016/j.arcontrol.2023.04.004
- Saavedra MD, Inthamoussou FA, Garelli F (2024) Model-free dynamic estimation of fore-aft and side-to-side wind turbine tower deflections. J Renew Sustain Energy 16(6):063308. https://doi.org/10.1063/5.0216741

- Scruggs J (2024) Wave energy conversion: the control design problem. In: Rahimpour MR (ed) Encyclopedia of renewable energy, sustainability and the environment, 1st edn. Elsevier, Oxford, pp 49–58. https://doi.org/10.1016/B978-0-323-93940-9.00239-5
- Stoica P, Moses RL et al (2005) Spectral analysis of signals, vol 452. CiteSeer, Princeton
- Szandała T (2020) Review and comparison of commonly used activation functions for deep neural networks. Bio-inspired neurocomputing. Springer, Berlin, pp 203–224
- Wang Q, Ren F, Li R (2024) Geopolitics and energy security: a comprehensive exploration of evolution, collaborations, and future directions. Human Soc Sci Commun 11(1):1–26. https://doi.org/10.1057/s41599-024-03507-2
- Werbos PJ (1990) Backpropagation through time: what it does and how to do it. Proc IEEE 78(10):1550–1560
- Zhang M, Yuan ZM, Dai SS, Chen M-L, Incecik A (2024a) LSTM RNN-based excitation force prediction for the real-time control of wave energy converters. Ocean Eng 306:118023. https://doi.org/ 10.1016/j.oceaneng.2024.118023
- Zhang Z, Qin J, Huang S, Liu Y, Xue G (2024b) Wave excitation force prediction for arrays of wave energy converters in directional waves. Ocean Eng 304:117884. https://doi.org/10.1016/j. oceaneng.2024.117884
- Zhao J, Huang F, Lv J, Duan Y, Qin Z, Li G, Tian G (2020) Do RNN and LSTM have long memory? In: Daumé III H, Singh A (eds) Proceedings of the 37th international conference on machine learning, vol 119, Virtual. PMLR, pp 11365–11375

Publisher's Note Springer Nature remains neutral with regard to jurisdictional claims in published maps and institutional affiliations.

